Model-Based Registration of *Ex Vivo* and *In Vivo* MRI of the Prostate Using Elastography*

Guy Nir*, *Student Member, IEEE*, Ramin S. Sahebjavaher, *Student Member, IEEE*, Piotr Kozlowski,
Silvia D. Chang, Ralph Sinkus, S. Larry Goldenberg, and Septimiu E. Salcudean, *Fellow, IEEE*

Abstract—Registration of histopathology to *in vivo* magnetic resonance imaging (MRI) of the prostate is an important task that can be used to optimize *in vivo* imaging for cancer detection. Such registration is challenging due to the change in volume and deformation of the prostate during excision and fixation. One approach towards this problem involves the use of an *ex vivo* MRI of the excised prostate specimen, followed by *in vivo* to *ex vivo* MRI registration of the prostate. We propose a novel registration method that uses a patient-specific biomechanical model acquired using magnetic resonance elastography to deform the *in vivo* volume and match it to the surface of the *ex vivo* specimen. The forces that drive the deformations are derived from a region-based energy, with the elastic potential used for regularization. The incorporation of elastography data into the registration framework allows inhomogeneous elasticity to be assigned to the *in vivo* volume. We show that such inhomogeneity improves the registration results by providing a physical regularization of the deformation map. The method is demonstrated and evaluated on six clinical cases.

Index Terms—Biomedical image processing, elastography, image registration, magnetic resonance imaging (MRI), prostate cancer.

I. INTRODUCTION

WITH an estimated number of 241 740 new cases and 28 170 deaths in 2012, prostate cancer is the most commonly diagnosed cancer and second most common cause of cancer death among American men [1]. In its early stages, prostate cancer has no symptoms and is usually suspected when a prostate-specific antigen (PSA) test has shown a significant increase and/or when a digital rectal examination (DRE) shows stiff nodules or an asymmetric gland. Diagnosis cannot be confirmed until a biopsy test is returned positive.

Noninvasive detection and localization of prostate cancer in medical imaging is an important, yet difficult task, and therefore the subject of many ongoing research studies. Benefits range from diagnosis of cancer to treatment planning and execution. An accurate localization of cancer may lead to less conservative treatments that reduce possible side effects such as impotence and urinary incontinence. Affected procedures may include brachytherapy and radical prostatectomy.

The most accurate image based characterization of prostate cancer to date is generated from multi-parametric magnetic resonance imaging (MRI) (see [2] and references therein). In order to evaluate the ability of *in vivo* MRI to localize and characterize prostate cancer, the tomographic images must be compared to the histopathological analysis of the prostate that provides the ground truth of cancer following prostatectomy. Thus, registration of 2-D histological sections to a 3-D *in vivo* MRI volume is required to find their spatial correspondence. Such slice-to-volume registration is challenging due to the intensity difference between the modalities, and the deformation the specimen undergoes during excision and fixation.

A few works have proposed registration of histopathology directly to *in vivo* MRI, e.g., [3] and [4]. However, as discussed in [5], typical sparse sectioning of histological slices do not allow an accurate reconstruction of the 3-D histological volume, which may result in a registration error. Thus, [5] proposes to employ a 2-D registration between histological slices and corresponding *in vivo* MRI volume slices that are manually chosen by an expert.

Recently, researchers have proposed the use of an *ex vivo* MRI of the prostate specimen [6], [7] as an intermediate modality between histopathology and *in vivo* MRI. Performed after excision and fixation, and just before sectioning, such *ex vivo* scan captures the shape of the deformed specimen, and can therefore be better aligned with the histological slices using only a rigid registration. Compared to the histological slices, the superior axial resolution of the *ex vivo* scan provides true 3-D modeling of the specimen that facilitates a nonrigid registration to the *in vivo* MRI.

Thus, the slice-to-volume registration of histological sections to *in vivo* MRI can be divided into two more tractable registrations of histopathology to *ex vivo* MRI, and *ex vivo* to *in vivo*

*G. Nir is with the Department of Electrical and Computer Engineering, University of British Columbia, Vancouver, BC, V6T 1Z4 Canada (e-mail: guynir@ece.ubc.ca).

R. S. Sahebjavaher and S. E. Salcudean are with the Department of Electrical and Computer Engineering, University of British Columbia, Vancouver, BC, V6T 1Z4 Canada.

P. Kozlowski is with the MRI Research Centre, University of British Columbia, Vancouver, BC, V6T 1Z3 Canada.

S. D. Chang is with the Department of Radiology, University of British Columbia, Vancouver, BC, V5Z 1M9 Canada.

R. Sinkus is with the Centre de Recherche Biomédicale Bichat-Beaujon (CRB3), Institut National de la Santé et de la Recherche Médicale (INSERM), Hôpital Beaujon, 92110 Clichy, France.

S. L. Goldenberg is with the Department of Urologic Sciences, University of British Columbia, Vancouver, BC, V5Z 1M9 Canada.

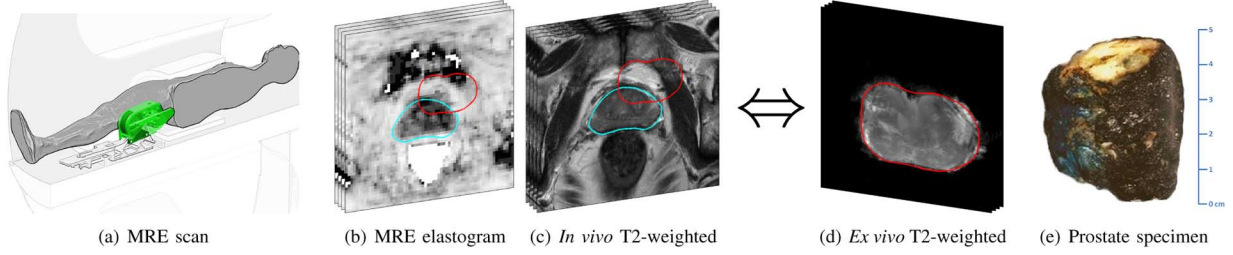| (a) MRE scan | (b) MRE elastogram | (c) *In vivo* T2-weighted | (d) *Ex vivo* T2-weighted | (e) Prostate specimen |

Fig. 1. Problem illustration. (a) Patients scheduled for radical prostatectomy undergo a preoperative transperineal MRE scan of the prostate. (b)–(c) The *in vivo* elastogram provides measured elasticity for each imaged voxel. (d)–(e) A 3-D model of the postoperative specimen, acquired from *ex vivo* MRI, should be registered to the *in vivo* MRI. Cross-sections of the unregistered *ex vivo* model (red) and the unknown *in vivo* prostate surface (cyan) are overlaid on slices.

MRI. The former registration can be solved with minimal error by approaches proposed, e.g., in [8] and [9], or by employing a multi-bladed cutting device [10] that mechanically constrains the prostate specimen during sectioning. For the latter registration, however, the authors in [6] propose only an interactive rigid registration between the *in vivo* and *ex vivo* volumes, which has been recognized to be a shortcoming [7].

It is the objective of the work described in this paper to develop and validate a method for an automatic and accurate 3-D registration between ex vivo and in vivo MRI. Fig. 1 illustrates the problem with typical images to be registered.

We propose a novel deformable registration approach, in which the *ex vivo* MRI volume of the prostate is segmented and treated as a reference model, and the *in vivo* MRI volume is treated as a deformable template with an underlying patient-specific biomechanical model. First, a similarity transformation (translation, rotation, and isotropic scaling) is employed to align the *ex vivo* and *in vivo* scans and correct for the change in volume. Following this initial alignment, an elastic registration is performed to match the template with the reference. Similar to [11], the deformation is driven by a region-based energy as the distance measure, and the elastic potential as a regularizer. Unlike [11], we deform the image in order to fit the model, and use an *inhomogeneous* biomechanical model, acquired from magnetic resonance elastography (MRE) [12], in our regularization term.

While potentially faster because of the much coarser discretization of images, biomechanical models derived from the finite element method (FEM), such as those employed in [13] and [14], require segmentation and meshing of the internal structure of the prostate and its surrounding anatomy. These steps are time consuming, often require user intervention and may generate errors that affect registration performance. Unlike FEM-based approaches, our method allows to solve the registration problem on a regular grid by using a variational approach and eliminates volume meshing. Such an approach was successfully employed in [15] for ultrasound image registration in prostate biopsy tracking.

The MRE technique that we use integrates relatively easily in a standard multi-parametric *in vivo* MRI session [Fig. 1(a)]. It involves the transperineal application of single- or multiple-tone harmonic mechanical excitation that generates shear waves in the prostate. The waves are measured by encoding the resulting displacements in the phase component of a synchronized MRI pulse sequence. Images, known as elastograms, that depict tissue elasticity or stiffness are generated from the imaged tissue displacements. With MRE, each voxel in the *in vivo* MRI is associated with the measured elasticity of the corresponding voxel in the elastogram. Additional details about the technique are given in [16] and Section V-A.

With few exceptions, e.g., [17]–[19], biomechanical models have been assigned arbitrary and typically constant elastic properties that are optimized to produce low registration errors. Even methods that do consider inhomogeneous elasticity for registration, express tissue inhomogeneity by setting values that are empirically found to work well. This is not always realistic and may result in inaccurate deformation maps.

In general, the current use of elastography in image processing is limited (see [20] for a review on applications in prostate imaging), and, in particular, the use of patient-specific elasticity maps for registration is new. We justify our approach by providing a novel quantitative analysis that shows the advantage in utilizing inhomogeneous elasticity for registration. We validate the method by presenting the results from synthetic and six patient data sets.

The remainder of this paper is organized as follows. Section II describes the theory and basic ideas behind the proposed methods. Section III presents a method for registering the *ex vivo* model to an *in vivo* volume using elastography. In Section IV we investigate the registration performance with respect to elastic inhomogeneity. In Section V, we provide experimental results of the proposed registration method on clinical data. Finally, we conclude in Section VI with a discussion and future research directions.

II. PRELIMINARIES

Here, and throughout the rest of this work, we use the following notations.

$x = (x_1, x_2, x_3)^T \in \mathbb{R}^3$	The 3-D spatial coordinates vector.
$\mathcal{D} \subseteq \mathbb{R}^3$	The 3-D domain on which the images are defined.
$R : \mathcal{D} \rightarrow \mathbb{R}$	The reference (*ex vivo*) image.
$T : \mathcal{D} \rightarrow \mathbb{R}$	The template (*in vivo*) image.
$\Phi_R : \mathbb{R}^3 \rightarrow \mathbb{R}$	A level set function that embeds the reference model.

$E_T : \mathcal{D} \to \mathbb{R}$ The elastogram associated with the template.

$u = (u_1, u_2, u_3)^T : \mathcal{D} \to \mathbb{R}^3$ A displacement field.

$\tilde{T}, \tilde{\Phi}_R$ The transformed template image and reference model.

$\| \cdot \|$ Euclidean (ℓ^2) norm.

A. Elastic Registration

We follow the general framework presented in [21], and provide a variational formulation of the nonrigid registration problem and the corresponding Euler–Lagrange equations that characterize a minimizer.

Let R, T denote the reference and template volumes, respectively, on a 3-D domain $\mathcal{D}$. Also, let u be a displacement field, such that the deformed template with respect to u is

$$\tilde{T}(x; u) = T(x - u(x)). \tag{1}$$

The registration problem is finding an admissible displacement field u, such that the deformed template $\tilde{T}$ is similar, in some sense, to the reference R. This problem is formulated as the minimization of the joint functional, or energy

$$\mathcal{J}[u; R, T] = \mathcal{F}[R, \tilde{T}(\cdot; u)] + \mathcal{S}[u] \tag{2}$$

where $\mathcal{F}$ represents a distance measure between the reference and the deformed template, and $\mathcal{S}$ is a metric that determines the smoothness or regularization of the displacements.

Common choices for a distance measure are sum of square differences (SSD), (normalized) cross-correlation, and (normalized) mutual information [22]. In [11], the authors proposed a region-based energy (see Section II-B) as the distance measure for a combined segmentation and registration. Their method maps a contour, which is extracted from a segmented template image, onto the reference image to provide the segmentation of the reference and its spatial correspondence with the template.

A variety of metrics have been proposed to regularize the deformations based on physical models, e.g., diffusion [23], fluid [24], and curvature [25] models. The authors in [26] and [27] proposed the linear elastic potential of the displacements as a regularizer, namely

$$\mathcal{S}[u] = \int_{\mathcal{D}} \left(\frac{\mu}{4} \sum_{j=1}^{3} \sum_{k=1}^{3} \left(\frac{\partial u_j}{\partial x_k} + \frac{\partial u_k}{\partial x_j} \right)^2 + \frac{\lambda}{2} (\mathrm{div}\, u)^2 \right) dx \tag{3}$$

where, from continuum mechanics, λ and μ are the Lamé parameters that reflect the elastic properties (μ is also known as the shear modulus).

In the variational approach, in order to minimize the functional (2), the Gâteaux derivative is computed with respect to u. This yields the Euler–Lagrange equation

$$\mathcal{A}[u](x) - f(x, u(x)) = 0 \tag{4}$$

where $-f$, also known as the (external) force, corresponds to the derivative of $\mathcal{F}$, and $\mathcal{A}[u]$, also known as the internal force, corresponds to the derivative of $\mathcal{S}$ and typically represents a partial differential operator. Thus, a minimizing displacement map should satisfy this equilibrium equation.

In the case of elastic potential as a regularizer, the Gâteaux derivative of (3) yields the Navier–Lamé operator

$$\mathcal{A}[u](x) = \mu \Delta u(x) + (\lambda + \mu) \nabla \mathrm{div}\, u(x) \tag{5}$$

for which the Euler–Lagrange equation, (4), is a second-order nonlinear PDE, also known as the elastostatic or Navier–Cauchy equation.

B. Region-Based Active Contours

Active contour models [28] have been extensively employed for image segmentation. In these methods, an initial segmenting surface is evolved in order to minimize an energy functional. Edge-based (classical) active contours, [29], [30], drive the surface to lock onto local maxima of image gradient magnitude values that typically characterize edges. The evolution of the surface in this case depends strictly on nearby pixels, and is therefore local. Region-based active contours, [31], [32], rely on regional statistics, such as sample mean and variance within the image, for the evolution of the segmentation surface, and direct its movement toward boundaries that are not necessarily defined by clear edges. Region-based models are global and tend to be robust to noise, since they take into account intensities within entire regions, rather than intensities of individual pixels.

The level set method, [33], [34], is an effective technique for implicit representation of evolving surfaces, frequently employed to implement active contours algorithms, since it inherently allows for cusps, corners and automatic topological changes. In the level set method, a surface (or contour in 2-D) is embedded as the zero level set of a function Φ. We will use the convention that Φ takes negative values in the region inside the surface and positive values in the region outside. A common choice for a level set function is the signed distance function, of which the value $\Phi(x)$ at each point x equals the Euclidean distance to its nearest point on the surface, multiplied by 1 or -1 according to the side of the surface x lies in.

Formulating energy functionals and their variations in the level set method often requires usage of the Heaviside function and the Dirac delta function, defined respectively by

$$\mathcal{H}(z) = \begin{cases} 1, & z \geq 0; \\ 0, & z < 0, \end{cases} \quad \text{and} \quad \delta(z) = \frac{d}{dz}\mathcal{H}(z).$$

In practice, regularized (smoothed) versions of $\mathcal{H}$ and δ are used, as suggested in [32], in order for the minimization process to be less local, thus increasing the chances of reaching a global minimizer, independent of the initial surface.

A popular region-based active contour model for image segmentation was proposed by Chan and Vese in [32]. In its level set formulation, the Chan–Vese algorithm minimizes the following energy functional with respect to the level set function Φ that embeds the segmenting surface

$$\mathcal{F}_{CV}[\Phi; T] = \int_{\mathcal{D}} (T - c_-)^2 \, \mathcal{H}(-\Phi) \, dx$$

$$+ \int_{\mathcal{D}} (T - c_+)^2 \, \mathcal{H}(\Phi) \, dx \tag{6}$$

(a) Initial   (b) Final (homogeneous)   (c) Final (inhomogeneous)
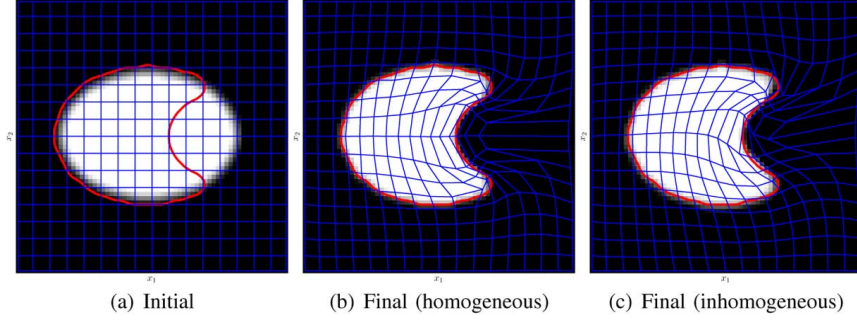
Fig. 2.   Registration of synthetic images. The reference contour (red) is overlaid on (a) the initial binary template, and (b)–(c) the warped template after registration using homogeneous/inhomogeneous elasticity. The grid (blue) illustrates the displacements.

where c_- and c_+ are the mean intensities of the image to be segmented, T, in the regions inside and outside the segmenting surface (i.e., the zero level set of Φ), respectively, given by

$$c_{\mp}[\Phi; T] = \frac{\int_{\mathcal{D}} T\mathcal{H}(\mp\Phi)\, dx}{\int_{\mathcal{D}} \mathcal{H}(\mp\Phi)\, dx}. \tag{7}$$

The minimization of (6) can be understood as partitioning the image into two homogeneous regions, by minimizing the variances of the intensities on the regions inside and outside the segmenting surface.

C. Model-Based Alignment

A nonrigid registration typically follows a rigid registration that corrects for the misalignment and change of coordinate systems between the two images. In this work we employ a model-based alignment based on an algorithm that was originally used in [35] for a shape-based segmentation.

Let Φ_R be a level set function that embeds the surface of a reference model, which was extracted by a segmentation of the reference image R. A similarity transformation in 3-D is defined by seven pose parameters: three translation values along each axis, three rotation angles about the axes, and one isotropic scale factor. Using a linear transformation of the spatial coordinates, the transformed model may be written as

$$\tilde{\Phi}_R(x; \Delta, \theta, \sigma) = \Phi_R(\sigma^{-1}\Theta^{-1}(x - \Delta)) \tag{8}$$

where Δ and θ are vectors that contain the translation and rotation parameters, respectively, σ is the scale, and Θ is the rotation matrix, which is determined by θ.

The authors in [35] propose to segment medical images by optimally fitting a model onto the image. They extract the principal modes of a training set that comprises different shapes of the target object, and obtain a parametric shape model by tuning the shape parameters, namely the coefficients in a linear combination of the principal modes. Their method minimizes region-based energy functionals in a level set formulation, among them the Chan–Vese energy in (6), with respect to the pose and shape parameters.

We consider a single element training set, in which the shape is the surface of the reference model. Since the minimization in this case is performed only with respect to the similarity pose

parameters, the method is degenerated into alignment of the model. The function to be minimized is therefore

$$F_{CV}(\Delta, \theta, \sigma) = \mathcal{F}_{CV}[\tilde{\Phi}_R(\cdot; \Delta, \theta, \sigma); T]. \tag{9}$$

The alignment algorithm employs gradient descent to minimize (9) by computing its derivatives with respect to the pose parameters. We refer the interested reader to [35] for details.

III. MODEL-BASED REGISTRATION USING INHOMOGENEOUS ELASTICITY

In our framework, high quality *ex vivo* images with a homogeneous background [as seen in Fig. 1(d)] allow a 3-D model of the prostate to be constructed easily by using either manual, semi- or fully automatic segmentation. In contrast, the *in vivo* images contain surrounding anatomy and tissue, with which the prostate blends. Thus, in our model-based registration, we take the *ex vivo* model as the reference, and the *in vivo* image as the template.

A. Model-Based Force

Motivated by the adequacy of region-based energies to delineate the prostate in MRI, as demonstrated in [35], we follow a model-based registration approach that incorporates a region-based energy as the distance measure between the template image and the reference model.

Specifically, we propose a distance measure which is based on the Chan–Vese energy in (6)

$$\mathcal{F}[u] = \frac{1}{2}\mathcal{F}_{CV}[\Phi_R; \tilde{T}(\cdot; u)] \tag{10}$$

where, as in Section II-C, Φ_R is a level set function that embeds the surface of the reference model. Note that in this formulation, the "segmenting" surface Φ_R is constant and the minimization is with respect to the displacement field.

Thus, in contrast to active contours segmentation methods and the registration approach in [11], here the image is deformed in order to fit the model, rather than the model surface to fit the image. This formulation allows for the inhomogeneous elasticity of the voxels in the template to regularize its deformations, as explained below.

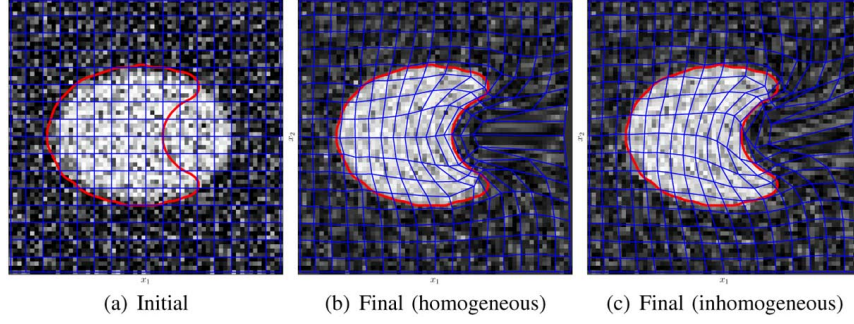(a) Initial   (b) Final (homogeneous)   (c) Final (inhomogeneous)

Fig. 3. Registration of noisy synthetic images. The reference contour (red) is overlaid on (a) the initial binary template with a Gaussian noise of 0.25 standard deviation, and (b)–(c) the warped template after registration using homogeneous/inhomogeneous elasticity. The grid (blue) illustrates the displacements.

By computing the Gâteaux derivative of (10), we have that the force associated with this energy is

$$f_{CV}(x, u(x)) = - \left[(T(x - u(x)) - \tilde{c}_-) \, \mathcal{H}(-\Phi_R) \right.$$
$$\left. + (T(x - u(x)) - \tilde{c}_+) \, \mathcal{H}(\Phi_R) \right] \nabla T(x - u(x)) \quad (11)$$

where, analogous to the discussion in Section II-B, $\tilde{c}_-$ and $\tilde{c}_+$ are the mean intensities of the deformed template image in the regions inside and outside the reference model.

Being derived mathematically, the magnitude of the forces acting on the template could be arbitrarily high and may force unrealistic deformation to bring it into the reference. However, using a scaling factor, we can normalize the forces such that their maximum magnitude inside the model is in the order of 0.1 N, which is physically plausible and within the same order of magnitude as the gravitational force on the prostate [36].

B. Inhomogeneous Regularization

As discussed in Section I, in most elastic registration algorithms, the Lamé parameters λ and μ are constant and chosen arbitrary. In elastography, we obtain measurements of the Young's modulus that is associated with each voxel of the template, E_T : $\mathcal{D} \to \mathbb{R}$. The corresponding Lamé parameters in this case are the functions given by

$$\lambda_T = \frac{E_T \cdot \nu}{(1 + \nu)(1 - 2\nu)} \quad \text{and} \quad \mu_T = \frac{E_T}{2(1 + \nu)} \quad (12)$$

with an (almost) incompressible Poisson ratio $\nu = 0.499$.

Thus, we modify (5) to contend with the inhomogeneous Lamé parameters

$$\mathcal{A}_T[u](x) = \mu_T(x - u(x))\Delta u(x)$$
$$+ (\lambda_T(x - u(x)) + \mu_T(x - u(x)))\nabla \text{div } u(x). \quad (13)$$

Note that λ_T and μ_T are deformed according to the template so as to "follow" its voxels. Also note that (13) is only a piecewise constant approximation of the problem. The nonapproximated operator, derived by taking the Gâteaux derivative of (3) with inhomogeneous Lamé parameters (see, e.g., [17] and [19]), contains terms with the gradients of the Lamé functions. Due to the noisy nature of elastography, the numerical calculation of these gradients is unreliable and the minimization is unstable. However, the approximation is justified by a typical "slow" spatial variation of the true elasticity (another option is
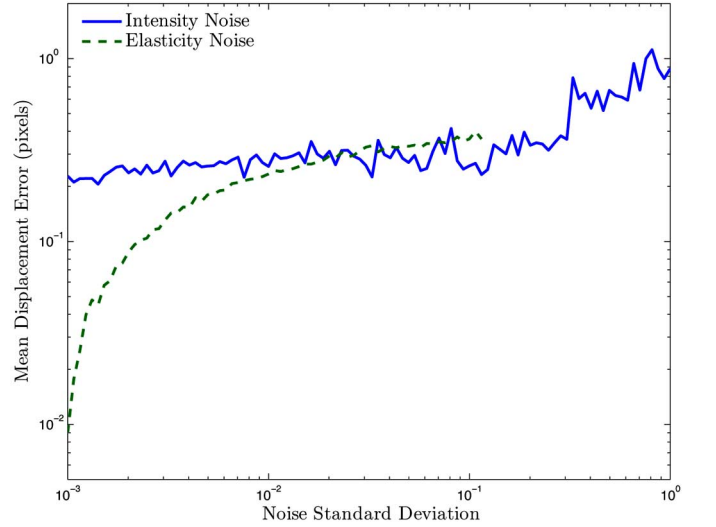

Fig. 4. Robustness to noise. The error is the mean Euclidean distance between the displacement maps resulting from noiseless and noisy registration of synthetic images, as seen in Figs. 2 and 3. The standard deviation of the noise represents the (inverse) signal-to-noise-ratio with respect to the ellipse (intensity and elasticity values of "1").

to employ a low-pass filtered elastogram and use the nonapproximated operator).

C. Energy Minimization

In order to solve the PDE (4) for the displacements u, with $\mathcal{A} = \mathcal{A}_T$ and $f = f_{CV}$, we follow a fixed-point iteration scheme [21], in which an initial (e.g., zero) displacement $u^{(0)}$ is assumed. We then solve

$$\mathcal{A}_T[u^{(k)}](x) = f_{CV}(x, u^{(k-1)}(x)), \quad k = 1, 2, \ldots \quad (14)$$

for $u^{(k)}$, until convergence. Since the elastic model relates to small (infinitesimal) deformations, we chain the resulting displacements at each iteration, as if the deformed template at each iteration is to be registered to the reference.

On a discrete grid, the technique is to first discretize $\mathcal{A}_T$ and f_{CV} using finite differences. Next, we generate a sparse convolution matrix A_T that corresponds to the operator $\mathcal{A}_T$ after discretization, such that (14) reads

$$A_T \underline{u}^{(k)} = \underline{f}_{CV}^{(k-1)} \quad (15)$$

(a) Initial   (b) Aligned   (c) Warped template   (d) Registered reference
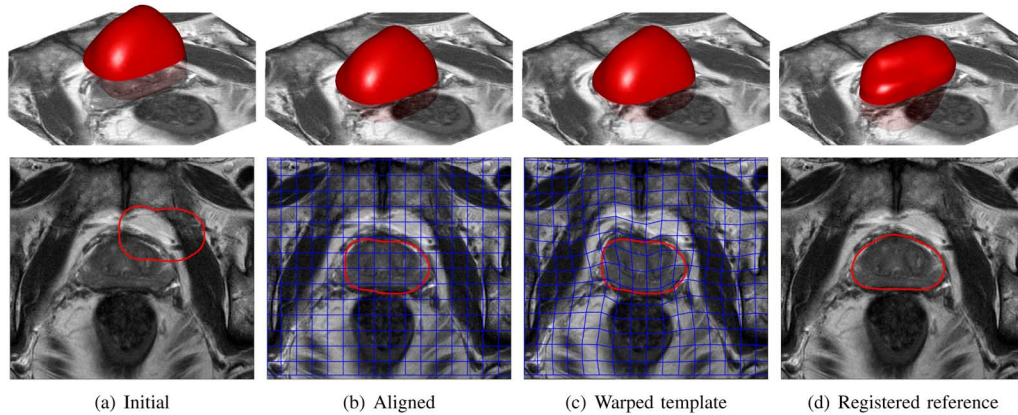
Fig. 5. Registration process. (a) The initial *ex vivo* reference model (red) is overlaid on a slice of the *in vivo* T2-weighted template image. (b) Translated, rotated and scaled model after using the model-based alignment. (c) Warped template after using the proposed model-based elastic registration. (d) Registered model after applying the inverse map. A 3-D view (top row) of the model, and a 2-D cross-section (bottom row) are shown.

where $\underline{f}_{CV}$ and $\underline{u}$ are column vectors that contain samples of the forces and (unknown) displacements on the discrete grid, respectively. The samples are ordered lexicographically by stacking the voxels of each component on top of one other to form one large column. Zero boundary conditions are assumed to compute the convolution matrix.

D. Synthetic Example

The proposed method is illustrated on a synthetic example in 2-D. Here, two binary images are being registered. The template is an ellipse with intensity values of "1" assigned to its inside and "0" outside. The reference is a similar but dented ellipse, of which the contour is used as the model.

In Fig. 2(a), the reference contour is overlaid on the initial template image. First, homogeneous elasticity was assigned to the template. Fig. 2(b) shows the final warped template (after 50 iterations). Notice the symmetry of the warped grid around the horizontal axis.

In the second example, the bottom half of the template was assigned three times stiffer elasticity values. Fig. 2(c) shows the final warped template in this case. As expected, the displacements are larger in the top half of the image.

Due to the employed region-based force, which takes into account region statistics rather than specific pixel values, the method is robust to noise. In Fig. 3 we see the same registration examples as before, but with a zero mean Gaussian noise added to the binary template image. The corresponding results (after 100 iterations) are shown in Fig. 3(a)–(c). Indeed, the results are very similar to the noiseless experiments [a slight grid asymmetry can be noticed in Fig. 3(b)].

In order to quantify the robustness to noise, we repeat the experiments for a Gaussian noise with different values of standard deviation. We evaluate both robustness to intensity variations, by adding the noise to the template, and robustness to elasticity variations, by adding the noise to the elasticity map. The resulting pixels' displacement map for each noisy registration is compared to the noiseless registration map. Fig. 4 plots the mean Euclidean norm (over all pixels) of the difference between the displacement maps against the corresponding standard deviation values of the noise.

The intensity noise and elasticity noise affect the results to a small extent (less than one pixel of error on average), up to standard deviation values of 0.1 (10% of noiseless intensity and elasticity). We see that intensity noise causes a constant error in the displacement. This is mostly due to small displacement errors in the background, and not due to errors in the large displacements around the object. The elasticity noise however, causes a logarithmic increase of the error. This is due to violation of the the "slow" varying assumption in the approximation of the Navier–Cauchy equation, (13).

For standard deviations above 0.1, the error caused by intensity noise increases, while elasticity noise yields convolution matrices A_T that are singular (to working precision), due to pixels with (almost) zero elasticity, causing the algorithm to fail. We also found a logarithmic relationship between the noise and the required number of iterations for convergence.

E. Clinical Example

Here, we describe the utilization of the proposed method for registration between an *ex vivo* model and the *in vivo* MRI volume and demonstrate the process on clinical data.

As a preprocessing step, we translate the *ex vivo* model to match its center with the center of the *in vivo* volume. Next, we employ the model-based approach described in Section II-C for fine alignment with respect to translations, scaling and rotations. Finally, we compute the residual nonrigid map between the aligned model and the image using the proposed model-based registration with inhomogeneous elasticity.

The registration process is illustrated in Fig. 5. Note that in Fig. 5(c), the template image is warped to fit the prostate inside the reference model. The inverse map is then applied to the rigidly aligned model in order to produce the registered *ex vivo* model on the coordinate system of the *in vivo* image, as seen in Fig. 5(d).

We note that in [35], the authors transformed the T2-weighted images by applying the gradient operator in order to increase intensity homogeneity inside the prostate and accentuate its boundaries for their region-based segmentation to work. In our case, we found the registration to perform better on the MRE
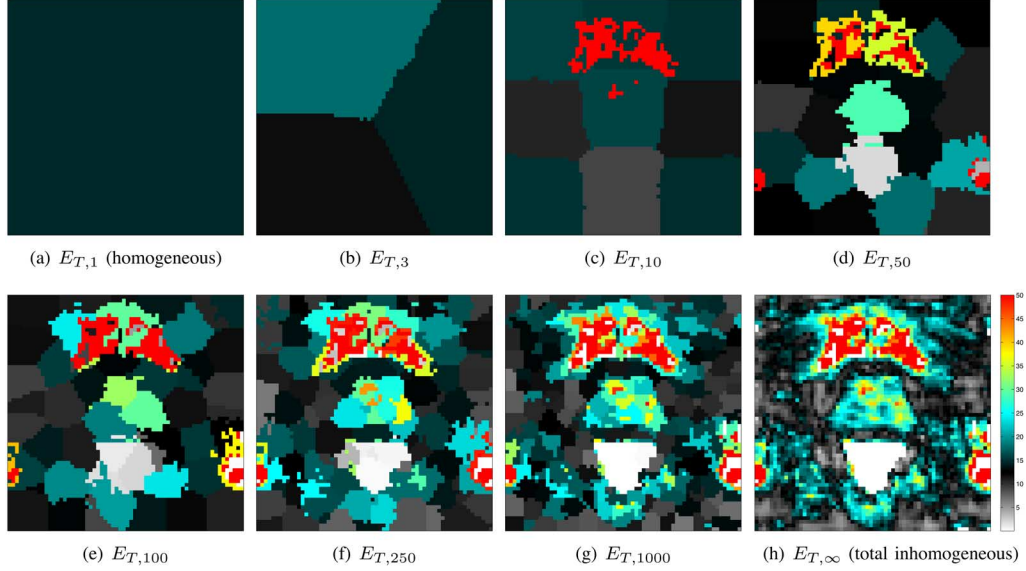
Fig. 6. Elastograms for different values of the inhomogeneity parameter. Intensity scale is in kilopascals.

(a) $E_{T,1}$ (homogeneous) (b) $E_{T,3}$ (c) $E_{T,10}$ (d) $E_{T,50}$

(e) $E_{T,100}$ (f) $E_{T,250}$ (g) $E_{T,1000}$ (h) $E_{T,\infty}$ (total inhomogeneous)

magnitude images (see Section V-A), and superimposed the results on the T2-weighted images.

IV. ELASTIC HOMOGENEITY VERSUS INHOMOGENEITY

In this section we provide analysis to show that inhomogeneous elasticity improves the registration performance. In order to do so, we degenerate the MRE measured elastogram, E_T, by employing the k-means clustering algorithm [37] with different values of k's.

The feature space to be clustered comprises the elasticity value, with the addition of the spatial coordinates x, in order to create geometrically connected clusters. The "points" to be clustered are therefore the feature vectors generated for each voxel. A clustered elastogram $E_{T,k}$ is created by applying the elasticity value of the centroid to each voxel in the corresponding cluster.

The extreme case of $k = 1$ yields a homogeneous elastogram, $E_{T,1} = \text{const}$, in which the intensity is the mean elasticity value. The other extreme, which we denote by $k \to \infty$, yields the original inhomogeneous elastogram, $E_{T,\infty} = E_T$. We therefore refer to k as the inhomogeneity parameter.

In fact, any value $k \geq N$, where N is the total number of voxels, and, in practice, due to repetitions in the quantized data, even lower k's, yield the same clustering as $k \to \infty$. Fig. 6 depicts a mid-gland slice of the elastograms, which correspond to the example case in Fig. 5, for selected values of the inhomogeneity parameter in the range between homogeneity and total inhomogeneity.

We repeatedly perform the registration described in Section III-E for different values of the inhomogeneity parameter, with respect to the resulting clustered elastogram. We run each registration until convergence to the same energy value that we have achieved in the original experiment. Therefore, the resulting warped templates look similar to each other and to the result in Fig. 5(c). However, as expected, the displacements that map each of the templates are different.

Fig. 7 shows the Euclidean norms of the displacement difference between the resulting maps that correspond to the inhomo-

geneity parameter values shown before. Specifically, Fig. 7(h) shows the difference between the total inhomogeneous and homogeneous registration maps on the mid-gland slice, and we may notice a difference of ~ 3.5 mm inside the prostate region.

The performance is evaluated for each registration through the volume overlap, in the sense of Dice's coefficient (16), between the registered *ex vivo* model and a manually segmented *in vivo* model, and through the distance between manually selected landmarks on the two modalities (see Section V-C). Fig. 8 shows these measures for different values of the inhomogeneity parameter.

Indeed, we identify the general trends that the volume overlap and the landmark error are, respectively, in direct and inverse proportion with the inhomogeneity parameter. We therefore conclude that performance improves when an inhomogeneous model is used. We note, however, that for two cases, the maximum volume overlap and minimum error were attained at $k = 250$ and $k = 500$ rather than $k \to \infty$. The reason for that is the noisy nature of the inhomogeneous elastogram that violates the "slow" varying assumption, as discussed in Section III-D.

Thus, setting a value for k that is too small leads to elastic homogeneity, while setting its value too high may lead to inaccurate regularization. In our experiments we take $k = 250$, since for greater values, when applicable, the improvement is not significant.

V. EXPERIMENTS

In this section we describe the acquisition of the data sets that were used in our study. We provide details on the imaging protocol, as well as on the implementation of the registration algorithm, its execution time and evaluation. Finally, we summarize the results of the registration experiments.

A. Data Acquisition

1) In Vivo Scan: After approval of the institutional ethics board and signed consents, six patients (mean age 65, range

(a) $\|u_{k=3} - u_{k=1}\|$ (b) $\|u_{k=10} - u_{k=3}\|$ (c) $\|u_{k=50} - u_{k=10}\|$ (d) $\|u_{k=100} - u_{k=50}\|$

(e) $\|u_{k=250} - u_{k=100}\|$ (f) $\|u_{k=1000} - u_{k=250}\|$ (g) $\|u_{k\to\infty} - u_{k=1000}\|$ (h) $\|u_{k\to\infty} - u_{k=1}\|$
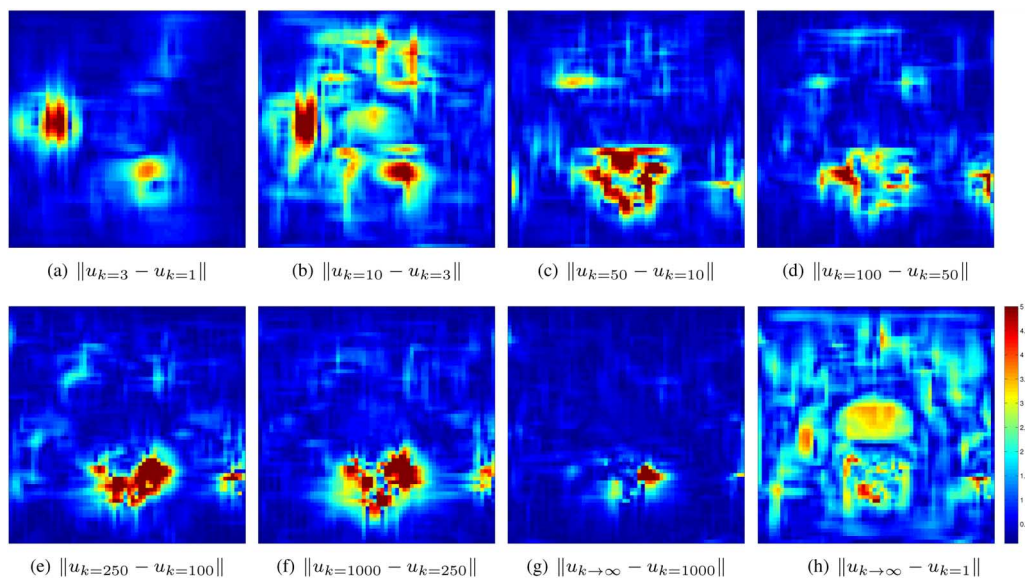
Fig. 7. Displacement difference maps resulting from registrations using different values of the inhomogeneity parameter. Intensity scale is in millimeters.
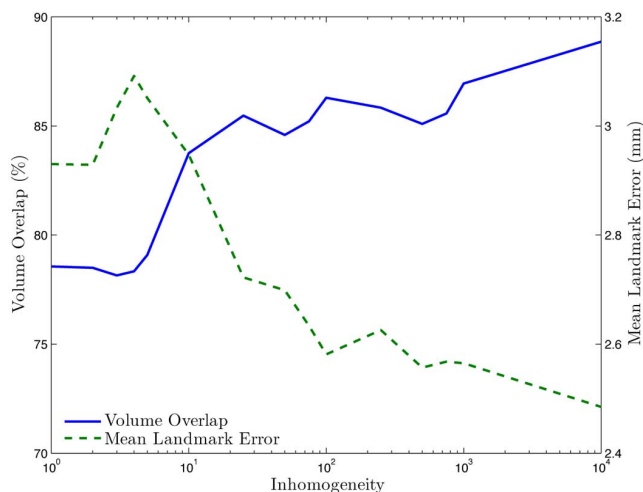

Fig. 8. Registration performance for different values of the inhomogeneity parameter.

TABLE I
MRE RESULTS: QUANTITATIVE SUMMARY OF ELASTICITY INSIDE
AND OUTSIDE THE PROSTATE. VALUES ARE IN KILOPASCALS

Case	Min.–Max. inside	Mean inside	Min.–Max. outside	Mean outside
1	$4.8 - 50.3$	19.5 ± 9.8	$1.6 - 75.3$	13.1 ± 6.0
2	$3.0 - 36.6$	17.7 ± 5.3	$1.4 - 79.6$	11.1 ± 5.2
3	$2.0 - 38.0$	13.7 ± 6.8	$1.0 - 36.4$	8.5 ± 4.5
4	$1.6 - 26.0$	11.6 ± 3.6	$1.3 - 53.1$	9.7 ± 5.3
5	$6.6 - 37.0$	21.0 ± 6.7	$1.9 - 79.2$	15.8 ± 9.0
6	$10.3 - 50.8$	24.0 ± 6.5	$2.8 - 54.5$	15.0 ± 8.2

acquisition. Each slice was cropped to accommodate 64×64 pixels around the prostate region for computational efficiency, and then processed offline to generate an elastogram similarly to the approach described in [39].

The quantitative elasticity values that were obtained are summarized in Table I. The range and mean elasticity were computed over the regions inside and outside (excluding the pubic bone) of the prostate boundary (manually chosen by an expert for the registration evaluation). The results demonstrate the inhomogeneity in elasticity and the fact that, in general, the prostate is stiffer (higher values) than its surrounding tissue. For other reported elasticity values of the prostate, see [16] and references therein.

In addition to the elastogram, an image was generated from the magnitude component of the MRE signal. This image, referred to as the magnitude image, is intrinsically aligned with the elastogram and provides complementary intensity information. An example slice of the magnitude image in Fig. 9(e) shows the intensity homogeneity inside the prostate, which is ideal for a region-based algorithm to be employed on. The scanning geometry, as given in the scanner output, determines the alignment of both the elastogram and the magnitude image with the T2-weighted volume.

2) Ex Vivo Scan: The postoperative *ex vivo* prostate specimen was fixed in 10% buffered formalin, typically for 72 h. It was then wrapped in a plastic bag, taped to a dedicated holder and scanned in a 7T system (Biospec, Bruker, Germany).

59–76 years old) who were scheduled for radical prostatectomy, underwent a preoperative *in vivo* T2-weighted scan followed by MRE scan in a 3T system (Achieva 3.0T, Philips, The Netherlands). A standard 6-channel cardiac coil with acceleration factor (SENSE) of 2 was used.

First, a sagittal scout image was acquired to ensure that the transperineal MRE driver is properly positioned at the beginning of the examination, as illustrated in Fig. 9(a). Then, a standard axial T2-weighted fast spin echo (FSE) sequence was acquired ($\text{TE}/\text{TR} = 86/2500$ ms, $\text{FOV} = 320 \times 320 \times 70$ mm^3, with 0.5 mm in-plane resolution and 2 mm slice thickness).

Next, a transperineal prostate MRE scan was acquired using a gradient echo sequence named eXpresso [38]. Eight phases were encoded with a mechanical excitation of 70 Hz applied to the perineum of the patient [16]. Wave images were acquired on a $128 \times 128 \times 24$ matrix with 2 mm isotropic voxel size. Fig. 9 shows an example slice of these wave images. The entire MRE scan lasted about 8 min for a 3-D displacement field

(a) Sagittal T2-weighted   (b) MRE phase 3/8   (c) MRE phase 5/8   (d) MRE phase 7/8   (e) MRE magnitude
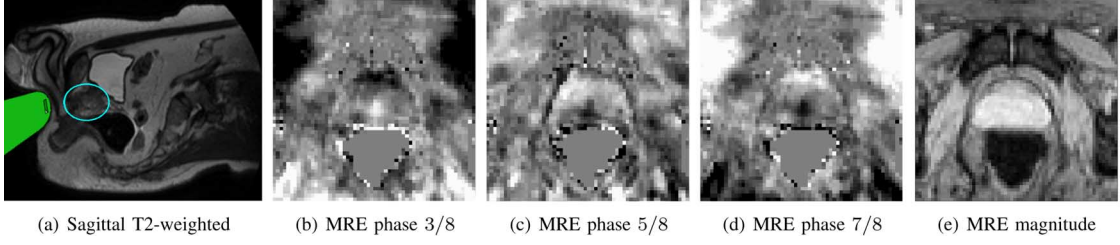
Fig. 9. MRE technique. (a) Illustration of the driver positioning (green), with the prostate region (cyan) overlaid on a sagittal scout image of the patient. (b)–(d) Three phases of displacements along the Y-axis, $\pi/2$ apart, depict wave propagation in the tissue, (e) The corresponding slice of the magnitude component image.

A rapid acquisition with relaxation enhancement (RARE) pulse sequence was used to acquire axial T2-weighted images (TE/TR $= 70/5000$ ms, FOV $= 70 \times 70 \times 42$ mm^3, with 0.2734 mm in-plane resolution and 2 mm slice thickness).

To extract the *ex vivo* model, the images were semi-automatically segmented by employing the region-based active contours algorithm described in Section II-B, with manual corrections by a radiologist that were required mainly due to artifacts caused by imaging of the wrapping bag around the specimen. We have then used Stradwin (Cambridge University, U.K.) [40], which employs [41], in order to generate a surface from the segmented *ex vivo* slices. We set the surface resolution and smoothing strength to "medium."

B. Implementation Details

We have implemented our registration method and tested it under MATLAB on a 2.93 GHz Quad Core CPU machine with 8 GB of RAM. It typically takes 100 iterations of rigid registration, and additional 100 iterations of nonrigid registration to reach convergence of the energy. The bottleneck of the algorithm is solving (15) for the displacement values. It involves finding $3 \times N$ unknowns in each iteration, where N is the total number of voxels. This is usually a large number and makes the algorithm computationally expensive.

In general, the inhomogeneity of the Lamé parameters yields sparse, but nonsymmetric and nonperiodic convolution matrices A_T, which do not allow numerical schemes to take advantage of their structure, e.g., as in [42] where the authors employ the fast Fourier transform (FFT) for fast inversion. Thus, an approximate solution of the problem is found by employing the biconjugate gradient method [43] for a fixed number of iterations, while keeping execution times within reason. We found 50 iterations to provide plausible results, which resulted in a total execution time of about 12 min for registering $64 \times 64 \times 24$ volumes on an unoptimized code.

C. Results

To evaluate the registration performance, we compare the final registered *ex vivo* model to an *in vivo* prostate model that was segmented manually by an expert on the T2-weighted slices. As a general performance indicator, we measure VO, the volume overlap between the registered and manual 3-D models in the sense of Dice's coefficient, i.e., twice the size of

the intersected volume divided by the sum of the sizes of the volumes. In the level set method, this can be formulated as

$$VO = \frac{2 \int_{\mathcal{D}} \mathcal{H}(-\tilde{\Phi}_R)\mathcal{H}(-\Phi_T)\,dx}{\int_{\mathcal{D}} \left(\mathcal{H}(-\tilde{\Phi}_R) + \mathcal{H}(-\Phi_T) \right)\,dx} \qquad (16)$$

where $\tilde{\Phi}_R$ and Φ_T are the level set functions embedding the registered (warped) model and the manual model, respectively. Similarly, in order to evaluate the performance at different regions of the prostate, we measure AO, which is the area overlap between cross-sections of the registered and manual models on slices from the base, mid-gland, and apex regions of the gland.

In addition, the expert has identified matching landmarks inside the prostate region on both the *ex vivo* and *in vivo* images. We measure the Euclidean distance between the registered *ex vivo* landmarks and their *in vivo* counterparts. Since our goal is to register (unknown) cancerous regions inside the prostate, these distances between landmarks provide us a good approximation of the target registration error (TRE).

Finally, in order to evaluate the improvement that was achieved by employing MRE, we repeated the experiments for all cases after assigning the voxels a homogenous elasticity value that is equal to the mean elasticity value inside the prostate (the elastogram region inside the expert's manual segmentation). Note that this experiment is different than the simulation with $k = 1$ in Section IV, where the mean elasticity of the entire field of view was used, and is expected to perform better since the elasticity inside the prostate is more relevant. We compare these homogeneous registration results to the inhomogeneous registration results.

Fig. 10 visualizes the inhomogeneous registration results. In Fig. 10(a), the surfaces of the registered and manual models of each case are shown in 3-D, together with the registered and manual landmarks. Fig. 10(b)–(d) shows cross-sections of the registered and manual models overlaid on selected slices from the base, mid-gland and apex regions of the prostate, respectively. Quantitative and statistical summaries of the registration results are presented in Table II and Fig. 11, respectively.

VI. DISCUSSION AND CONCLUSION

We have presented a method for an automatic model-based registration of *ex vivo* and *in vivo* prostate MRI. The method can be fused with established methods that consider registration of *ex vivo* MRI and histological sections, in order to recover the spatial correspondence between histopathology and the *in vivo*
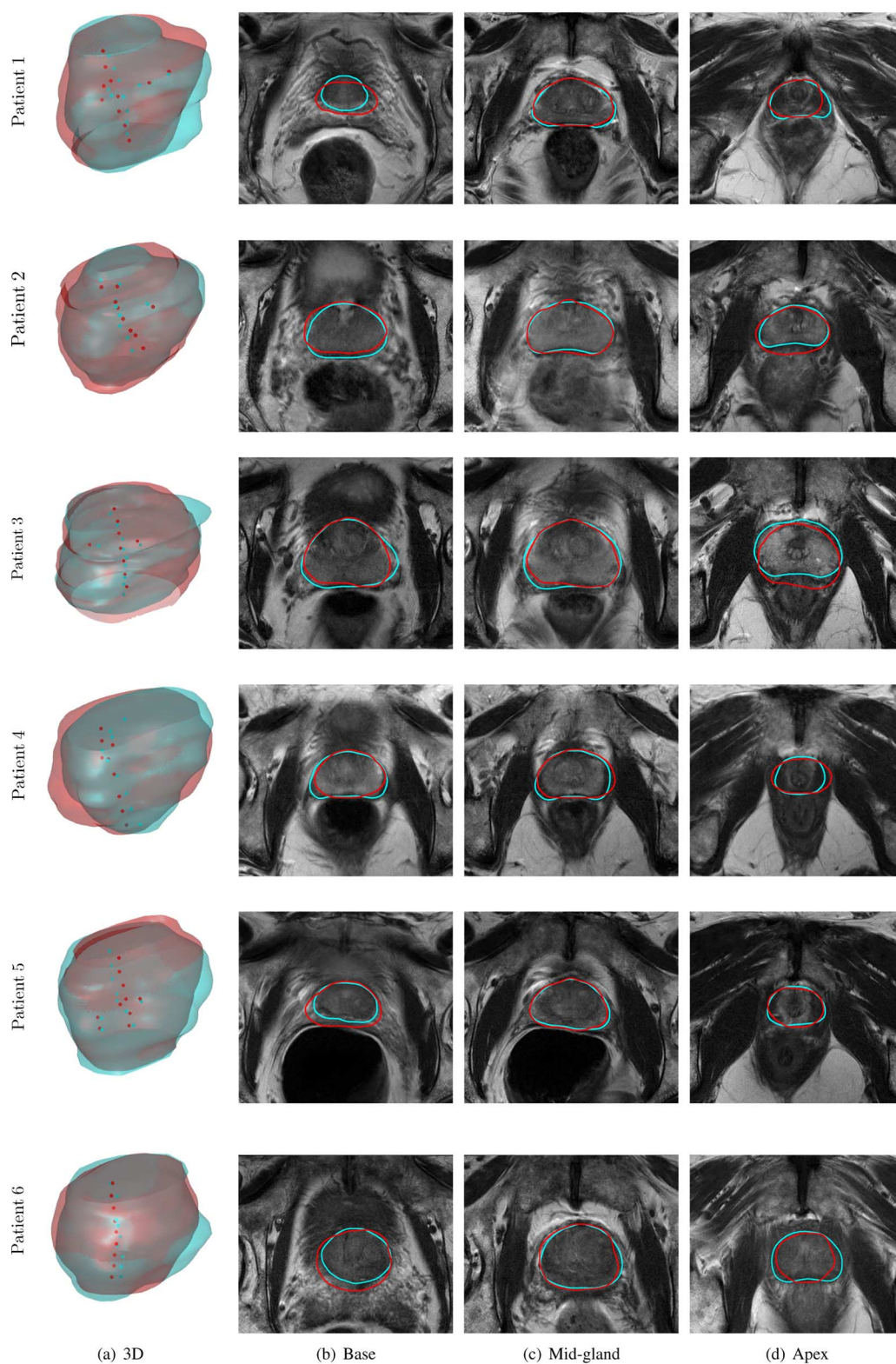
Fig. 10. Inhomogeneous registration results. The registered *ex vivo* reference model (red) and a manually segmented model (cyan) of the *in vivo* T2-weighted template image. Spheres in column (a) represent registered and manually marked landmarks. Columns (b)–(d) show cross-sections of the models overlaid on selected T2-weighted slices from the base, mid-gland and apex regions of the prostate.

scan. Since histopathology of the prostate provides the ground truth cancerous and noncancerous regions, a correct mapping of these regions onto an MRI volume allows characterization of prostate cancer on co-registered multi-parametric MRI, and

may provide training and validation sets for a classifier that produces cancer probability maps on preoperative images. Typical training sets may include 10–20 cases, and validation sets may include 50–100 cases. Focusing on regions with high probability

TABLE II
REGISTRATION RESULTS: QUANTITATIVE SUMMARY

| Case	Inhomogeneous Elasticity					Homogeneous Elasticity	
	Base AO (%)	Mid-gland AO (%)	Apex AO (%)	VO (%)	Error (mm)	VO (%)	Error (mm)
1	77.7 ± 4.5	91.0 ± 2.3	88.3 ± 0.8	87.5	2.5 ± 0.8	85.3	3.1 ± 1.1
2	76.6 ± 10.9	92.4 ± 2.6	78.1 ± 7.8	85.9	1.5 ± 0.6	84.0	2.8 ± 0.7
3	90.3 ± 0.6	92.1 ± 3.0	78.9 ± 2.4	87.3	3.2 ± 1.0	82.9	3.1 ± 0.8
4	83.5 ± 6.0	83.5 ± 4.7	76.0 ± 2.9	81.6	4.3 ± 2.5	76.9	5.2 ± 3.6
5	90.0 ± 4.9	93.5 ± 2.5	89.9 ± 1.0	88.1	2.3 ± 1.3	84.1	2.5 ± 1.2
6	85.7 ± 2.3	91.2 ± 2.4	79.4 ± 9.3	86.9	4.1 ± 1.4	82.9	5.5 ± 2.3
mean	83.4 ± 7.7	90.8 ± 4.0	81.8 ± 7.1	86.2 ± 2.4	3.1 ± 1.4	82.7 ± 3.0	3.72 ± 1.9
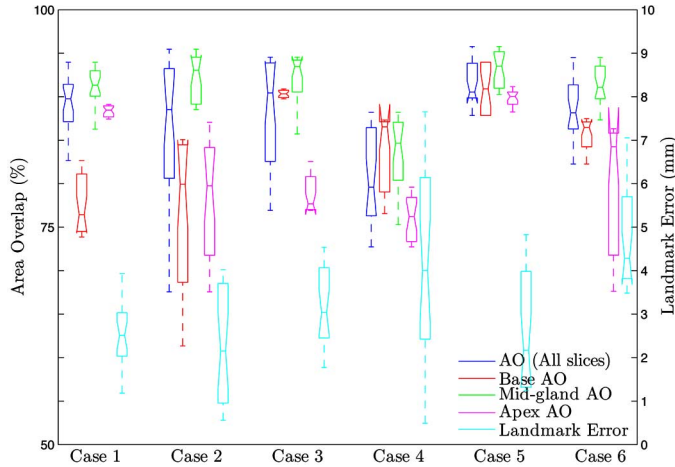
Fig. 11. Inhomogeneous registration results: Statistical summary of the resulting area overlap (AO) among slices, and the landmark error.

of cancer could impact treatments such as brachytherapy and radical prostatectomy, and reduce possible side effects such as impotence and urinary incontinence.

The proposed method aligns a model of the prostate, constructed from the *ex vivo* MRI, onto the *in vivo* volume, and then warps the *in vivo* volume so as to fit the aligned model. A variational approach has been used to derive the registration algorithm using a region-based active contour model in a level set formulation. The method was first demonstrated on synthetic images to evaluate its robustness to noise in the data, and was further tested and evaluated on six clinical cases by comparing the registered *ex vivo* model to manual segmentations of the *in vivo* volume, and by computing the distances between registered landmarks on the two modalities.

Our approach employs an MRE scan that allows measurement and assignment of elastic properties of the tissue to corresponding voxels in the image. In turn, this provides an implicit modeling of the prostate and its surrounding anatomical structures that allows warping the *in vivo* volumetric image onto the *ex vivo* model in a physical manner. Moreover, we found the MRE magnitude image to be an excellent candidate for the region-based approach due to its intensity homogeneity within the prostate. Often regarded as a by-product of the MRE process and ignored, this is the first paper to employ the magnitude image for registration.

Thus, *the main contributions of this work are the incorporation of an MRE scan into the registration framework, and its*

employment as both an imaging modality that drives the deformation, and as a biomechanical model that regularizes the deformation.

While the most valuable information is pertaining to the prostate itself, utilizing the elasticity of both the prostate and its surrounding tissue is more likely to result in a mapping that portrays the actual displacement of the voxels within the prostate. This is attributable to the fact that most deformation occurs *in vivo* (*ex vivo* deformation is typically manifested as shrinkage and corrected by scaling), and is therefore governed by the *in vivo* elasticity and interaction of the prostate with its surrounding anatomy. Indeed, we have showed that this approach yields improved registration as opposed to applying a constant elasticity value to the volume, and that, in general, the performance improves with the inhomogeneity of elasticity inside and outside of the prostate. To the best of our knowledge, no such study has been conducted thus far. We note that an *ex vivo* measurement of the elasticity, although might be technically simpler, reflects the much stiffer elasticity of the post-fixation specimen which is irrelevant to the deformation.

In addition, our approach does not require segmentation and meshing of the *in vivo* anatomy, as opposed to explicit FEM-based modeling approaches. Although, as discussed above, the designated application of classification requires a limited number of cases, segmentation and meshing can still consume a significant amount of time. On the other hand, MRE is fast and easily integrated into the *in vivo* MRI protocol. Even in case that FEM is to be employed instead of our approach, MRE could benefit the chosen algorithm by providing the model with patient-specific elasticity.

The performance of the registration, and the significance of its improvement using MRE, should be evaluated with respect to the designated application. The mean registration error that was achieved during the experiments is within the tumor diameter that MRI is reported to detect and characterize prostate cancer [44], and within the size of most clinically significant lesions that are marked during histopathology analysis ($\sim 10 \pm 5$ mm [45]). Thus, in our case, the method is suitable for mapping of these tumors on the *in vivo* MRI. However, the registration might not be accurate enough to characterize early stage tumors that are considered in, e.g., training a classifier for an image-guided biopsy application. Since MRE depends on fairly complex modulus reconstruction, we expect the registration results to improve with the developments in our reconstruction methods.

As other registration techniques, the proposed algorithm performs better on the mid-gland region of the prostate. This finding is due to the ambiguity in contouring the prostate around the base and apex on the *ex vivo* and *in vivo* images, that impacts the fidelity of both the model and evaluation in these regions. In future work, we may utilize the intensity similarity between *in vivo* and *ex vivo* T2-weighted MRI to derive forces from intensity-based distance measures, e.g., mutual information. This may eliminate the required segmentation of the *ex vivo* volume, and improve speed and accuracy.

A disadvantage of the proposed approach is that the *ex vivo* MRI scan is time consuming, expensive and not accessible. However, as discussed above, the proposed method should be employed on a limited number of cases for the designated application. Moreover, as discussed in Section I, methods that propose direct registration between *in vivo* MRI to histopathology require either dense sectioning of histological slices [3], or manual selection of corresponding slices [5]. Another direct approach, proposed in [46] and [47], generates a patient-specific mold, based on the (nondeformed) *in vivo* prostate, to preserve sectioning orientation. Thus, current direct registration methods can be just as time consuming as the *ex vivo* scan, while being more user-dependent and error-prone.

We note, however, that since the *ex vivo* scan in our approach is used only to acquire a model of the specimen, a direct registration to histopathology is still possible using our method by using a 3-D model reconstruction based on the histological slices, provided that their sectioning is dense enough. In addition, other *ex vivo* imaging modalities, which are more accessible than MRI, can be employed. In fact, an ultrasound generated *ex vivo* model may be combined with methods such as [48] to register the *ex vivo* scan to histology following our method. Thus, our framework is general and can be fitted into different workflows.

The current implementation does not allow real-time performance, which is not a requirement in the case of cancer characterization. The execution times are in the order of minutes, so multiple registrations can be processed on the background in a typical clinical scenario to provide a reasonable throughput. Another current limitation is the assumption of small deformations. Although the residual deformations are small after a similarity transformation, we may still consider nonlinear elasticity for future work in order to contend with large deformations of the prostate, e.g., in case of employing a transrectal coil during image acquisition.

REFERENCES

[1] Cancer facts & figures 2012 Am. Cancer Soc. [Online]. Available: http://www.cancer.org
[2] P. Kozlowski *et al.*, "Combined prostate diffusion tensor imaging and dynamic contrast enhanced MRI at 3t-quantitative correlation with biopsy," *Magn. Reson. Imag.*, vol. 28, no. 5, pp. 621–628, 2010.
[3] Y. Ou, D. Shen, M. Feldman, J. Tomaszewski, and C. Davatzikos, "Non-rigid registration between histological and MR images of the prostate: A joint segmentation and registration framework," in *IEEE Comput. Soc. Conf. Comput. Vis. Pattern Recognit. Workshops*, 2009, pp. 125–132.
[4] Y. Zhan, Y. Ou, M. Feldman, J. Tomaszewski, C. Davatzikos, and D. Shen, "Registering histological and MR images of prostate for image-based cancer detection," *Acad. Radiol.*, vol. 14, no. 11, pp. 1367–1367, 2007.
[5] J. Chappelow, B. Bloch, N. Rofsky, E. Genega, R. Lenkinski, W. De-Wolf, and A. Madabhushi, "Elastic registration of multimodal prostate MRI and histology via multiattribute combined mutual information," *Med. Phys.*, vol. 38, no. 4, pp. 2005–2005, 2011.
[6] A. Ward, C. Crukley, C. McKenzie, J. Montreuil, E. Gibson, J. Gomez, M. Moussa, G. Bauman, and A. Fenster, "Registration of in vivo prostate magnetic resonance images to digital histopathology images," in *Prostate Cancer Imag. Computer-Aided Diagnosis, Prognosis, Intervent.*, 2010, pp. 66–76.
[7] A. Ward *et al.*, "Prostate: Registration of digital histopathologic images to in vivo MR images acquired by using endorectal receive coil," *Radiology*, vol. 263, no. 3, pp. 856–864, 2012.
[8] E. Gibson, C. Crukley, M. Gaed, J. Gómez, M. Moussa, J. Chin, G. Bauman, A. Fenster, and A. Ward, "Registration of prostate histology images to ex vivo MR images via strand-shaped fiducials," *J. Magn. Reson. Imag.*, vol. 36, no. 6, pp. 1402–1412, 2012.
[9] S. Kimm, T. Tarin, J. Lee, B. Hu, K. Jensen, D. Nishimura, and J. Brooks, "Methods for registration of magnetic resonance images of ex vivo prostate specimens with histology," *J. Magn. Reson. Imag.*, vol. 36, no. 1, pp. 206–212, 2012.
[10] B. Drew, E. Jones, S. Reinsberg, A. Yung, S. Goldenberg, and P. Kozlowski, "Device for sectioning prostatectomy specimens to facilitate comparison between histology and in vivo MRI," *J. Magn. Reson. Imag.*, vol. 32, no. 4, pp. 992–996, 2010.
[11] C. L. Guyader and L. Vese, "A combined segmentation and registration framework with a nonlinear elasticity smoother," *Comput. Vis. Image Understand.*, vol. 115, no. 12, pp. 1689–1709, 2011.
[12] R. Muthupillai *et al.*, "Magnetic resonance elastography by direct visualization of propagating acoustic strain waves," *Science*, vol. 269, no. 5232, pp. 1854–1857, 1995.
[13] A. Bharatha *et al.*, "Evaluation of three-dimensional finite element-based deformable registration of pre-and intraoperative prostate imaging," *Med. Phys.*, vol. 28, pp. 2551–2551, 2001.
[14] R. Alterovitz, K. Goldberg, J. Pouliot, I. Hsu, Y. Kim, S. Noworolski, and J. Kurhanewicz, "Registration of MR prostate images with biomechanical modeling and nonlinear parameter estimation," *Med. Phys.*, vol. 33, pp. 446–446, 2006.
[15] M. Baumann, P. Mozer, V. Daanen, and J. Troccaz, "Prostate biopsy tracking with deformation estimation," *Med. Image Anal.*, vol. 16, no. 3, pp. 562–576, 2012.
[16] R. S. Sahebjavaher, A. Baghani, M. Honarvar, R. Sinkus, and S. E. Salcudean, "Transperineal prostate MR elastography: Initial in-vivo results," *Magn. Reson. Med.*, vol. 69, no. 2, pp. 411–420, 2013.
[17] C. Davatzikos, "Spatial transformation and registration of brain images using elastically deformable models," *Comput. Vis. Image Understand.*, vol. 66, pp. 207–222, 1997.
[18] H. Lester, S. Arridge, K. Jansons, L. Lemieux, J. Hajnal, and A. Oatridge, "Non-linear registration with the variable viscosity fluid algorithm," in *Information Processing in Medical Imaging*. New York: Springer, 1999, pp. 238–251.
[19] S. Kabus, A. Franz, and B. Fischer, "Spatially varying elasticity in image registration," *Methods Inf. Med.*, vol. 46, no. 3, pp. 287–291, 2007.
[20] S. E. Salcudean, R. S. Sahebjavaher, O. Goksel, A. Baghani, S. S. Mahdavi, G. Nir, R. Sinkus, and M. Moradi, "Biomechanical modeling of the prostate for procedure guidance and simulation," in *Soft Tissue Biomechanical Modeling for Computer Assisted Surgery*, ser. Studies in Mechanobiology, Tissue Engineering and Biomaterials, Y. Payan, Ed. Berlin, Germany: Springer, 2012, vol. 11, pp. 169–198.
[21] J. Modersitzki, *Numerical Methods for Image Registration*. New York: Oxford Univ. Press, 2004.
[22] P. Viola and W. M. Wells, III, S. Shafer, A. Blake, and K. Sugihara, Eds. , "Alignment by maximization of mutual information," in *IEEE Int. Conf. Comput. Vis.*, 1995, pp. 16–23, IEEE Computer Society Press.
[23] B. K. P. Horn and B. G. Schunck, "Determining optical flow," *Artif. Intell.*, vol. 17, pp. 185–203, 1981.
[24] G. E. Christensen, R. D. Rabbit, and M. I. Miller, "Deformable templates using large deformation kinematics," *IEEE Trans. Med. Imag.*, vol. 5, no. 10, pp. 1435–1447, Oct. 1996.
[25] B. Fischer and J. Modersitzki, "A unified approach to fast image registration and a new curvature based registration technique," *Lin. Alg. Appl.*, vol. 380, pp. 107–124, 2004.
[26] C. Broit, "Optimal registration of deformed images," Ph.D. dissertation, Comput. Inf. Sci. Dept., Univ. Pennsylvania, Philadelphia, 1981.
[27] R. Bajcsy and S. Kovacic, "Multiresolution elastic matching," *Comput. Vis. Graph. Image Proc.*, vol. 46, pp. 1–21, 1989.

[28] M. Kass, A. Witkin, and D. Terzopoulos, "Snakes: Active contour models," *Int. J. Comput. Vis.*, vol. 1, no. 4, pp. 321–331, 1988.

[29] V. Caselles, R. Kimmel, and G. Sapiro, "Geodesic active contours," *Int. J. Comput. Vis.*, vol. 22, no. 1, pp. 61–79, 1997.

[30] S. Kichenassamy, A. Kumar, P. Olver, A. Tannenbaum, and A. Yezzi, "Gradient flows and geometric active contour models," in *Int. Conf. Comput. Vis.*, 1995, pp. 810–815.

[31] A. Yezzi, A. Tsai, and A. Willsky, "A statistical approach to snakes for bimodal and trimodal imagery," in *Proc. Int. Conf. Comput. Vis.*, 1999, vol. 2, pp. 898–903.

[32] T. Chan and L. Vese, "Active contours without edges," *IEEE Trans. Image Process.*, vol. 10, no. 2, pp. 266–277, Feb. 2001.

[33] S. Osher and J. A. Sethian, "Fronts propagating with curvature dependent speed: Algorithms based on hamilton-jacobi formulations," *J. Comp. Phys.*, vol. 79, pp. 12–49, 1988.

[34] J. A. Sethian, *Level Set Methods and Fast Marching Methods Evolving Interfaces in Computational Geometry, Fluid Mechanics, Computer Vision, and Materials Science*, 2nd ed. New York: Cambridge Univ. Press, 1999.

[35] A. Tsai, A. Yezzi Jr., W. Wells, C. Tempany, D. Tucker, A. Fan, W. Grimson, and A. Willsky, "A shape-based approach to the segmentation of medical imagery using level sets," *IEEE Trans. Med. Imag.*, vol. 22, no. 2, pp. 137–154, Feb. 2003.

[36] F. Taquee, O. Goksel, S. Mahdavi, M. Keyes, W. Morris, I. Spadinger, and S. Salcudean, "Deformable prostate registration from MR and TRUS images using surface error driven FEM models," *Proc. SPIE*, vol. 8316, pp. 831612–831612, 2012.

[37] R. O. Duda, P. E. Hart, and D. G. Stork, *Pattern Classification*, 2nd ed. New York: Wiley-Interscience, 2001.

[38] R. S. Sahebjavaher, P. Garteiser, B. Van Beers, S. E. Salcudean, and R. Sinkus, "Rapid 3-D motion-encoding using spoiled FFE: Application towards multi-frequency MR rheology in liver," in *Eur. Soc. Magn. Reson. Med. Biol.*, 2011, pp. 124–124.

[39] R. Sinkus, J. Lorenzen, D. Schrader, M. Lorenzen, M. Dargatz, and D. Holz, "High-resolution tensor MR elastography for breast tumour detection," *Phys. Med. Biol.*, vol. 45, pp. 1649–1649, 2000.

[40] G. M. Treece, R. W. Prager, and A. H. Gee, Stradwin 4.4 U.K., Med. Imag. Group, Mach. Intell. Lab., Cambridge Univ. [Online]. Available: http://mi.eng.cam.ac.uk/~rwp/stradwin

[41] G. M. Treece, R. W. Prager, and A. H. Gee, "Regularised marching tetrahedra: Improved iso-surface extraction," *Comput. Graph.*, vol. 23, no. 4, pp. 583–598, 1999.

[42] B. Fischer and J. Modersitzki, "Fast inversion of matrices arising in image processing," *Num. Algor.*, vol. 22, no. 1, pp. 1–11, 1999.

[43] W. H. Press, S. A. Teukolsky, W. T. Vetterling, and B. P. Flannery, *Numerical Recipes 3rd Edition: The Art of Scientific Computing*, 3rd ed. New York: Cambridge Univ. Press, 2007.

[44] A. Kirkham, M. Emberton, and C. Allen, "How good is MRI at detecting and characterising cancer within the prostate?," *Eur. Urol.*, vol. 50, no. 6, pp. 1163–1175, 2006.

[45] L. Eichelberger, M. Koch, J. Daggy, T. Ulbright, J. Eble, and L. Cheng, "Predicting tumor volume in radical prostatectomy specimens from patients with prostate cancer," *Am. J. Clin. Pathol.*, vol. 120, no. 3, pp. 386–391, 2003.

[46] V. Shah, T. Pohida, B. Turkbey, H. Mani, M. Merino, P. Pinto, P. Choyke, and M. Bernardo, "A method for correlating in vivo prostate magnetic resonance imaging and histopathology using individualized magnetic resonance-based molds," *Rev. Sci. Instrum.*, vol. 80, pp. 104301–104301, 2009.

[47] H. Trivedi *et al.*, "Use of patient-specific MRI-based prostate mold for validation of multiparametric MRI in localization of prostate cancer," *Urology*, vol. 79, no. 1, pp. 233–239, 2012.

[48] L. Taylor, B. Porter, G. Nadasdy, P. di Sant'Agnese, D. Pasternack, Z. Wu, R. Baggs, D. Rubens, and K. Parker, "Three-dimensional registration of prostate images from histology and ultrasound," *Ultrasound Med. Biol.*, vol. 30, no. 2, pp. 161–168, 2004.